Advanced Optical Materials / Volume 12, Issue 5 / 2301827

Research Article | Full Access

Significantly Boosted Upconversion Emission in Cryogenic Er@Yb@Y Core–Shell–Shell Nanostructures

Enhui Wang, Wei Wang, Lujun Niu, Yansong Feng, Haifeng Zhao, Yongshi Luo, Ligong Zhang, Qiqing Li, Haoran Chen, Yulei Chang, Langping Tu, Hong Zhang, Jing Zuo

First published: 28 September 2023
https://doi-org.fgul.idm.oclc.org/10.1002/adom.202301827

Abstract

Recent advances reveal that due to the cross-relaxation restriction, impressive upconversion (UC) enhancement (≈100-folds) can be achieved in cryogenic Er^{3+}-rich core-inert shell nanostructures (e.g., $NaErF_4$@$NaYF_4$), which opens up exciting opportunities in diverse frontier applications. However, further promotion of UC intensity is still highly desired, in which the rational design of nanostructures can play a key role. Herein, it is demonstrated that adopting an active shell design will constantly benefit the UC within a wide temperature range (40–300 K). Specifically, through constructing the luminescent core@active shell@inert shell sandwich nanostructure (e.g., $NaErF_4$@$NaYbF_4$@$NaYF_4$), 8.3–73-folds UC enhancement will be achieved (taking the corresponding core@inert shell structures as competitors). Moreover, from spectral-domain and time-domain spectroscopic experiments, the relevant UC enhancement is convincingly attributed to a temperature-dependent energy injection process (from the active shell to the luminescent core). More interestingly, the unique property of the material makes a temperature-induced high-level encryption application possible, which is obtained by employing the nanomaterials on a quick response (QR) code. These results not only deepen the UC mechanism in multi-layer nanostructures, but also introduce an expanded dimension (via low temperatures) in information security.

1 Introduction

Due to the unique properties, such as large anti-Stokes shift, high chemical stability, sharp emission peaks, and low toxicity,[1] lanthanide (Ln) doped upconversion nanoparticles

(UCNPs) have attracted numerous attention in diverse fields,[2] including multi-modal bioimaging,[3] photodynamic therapy,[3, 4] 3D display,[5] anti-counterfeiting,[6] optogenetics,[7] and super-resolution imaging.[8] However, the critical bottleneck, i.e., insufficient upconversion (UC) brightness, still seriously hinders the further development of these materials.[9] Therefore, recent advances more and more focus on the topic of UC efficiency promotion.[1, 10] Especially for the nanosized UC systems, whose efficiency has been reported within the range of 0.01–5%,[11] thus leaving a huge room for further improvement.

An exciting breakthrough for UC material in recent years is the exploitation of active Ln high-level-doping nanostructures.[12] Specifically, it is found that the optimal doping concentration of active Ln ions (sensitizer or activator) in nanosystems is not always an invariant constant. Instead of that, the optimized concentrations are strongly related to the boundary conditions of the nanosystems. Therefore, via employing targeted strategies (e.g., high excitation irradiance,[13] dye sensitization,[14] surface passivation,[10, 15] and heterogeneous nanostructure design[16]) to carefully tailor the particular excitation/emission conditions in some rationally designed nanostructures, the negative "concentration quenching" effect on Ln can be efficiently restricted.[12] As a result, the optimal doping concentrations of active Ln ions (e.g., Er^{3+}, Yb^{3+}, Tm^{3+}, Ho^{3+}, Nd^{3+}), as well as the UC efficiency of relevant nanomaterials, are able to be significantly promoted 1–3 orders of magnitude.

One typical example is the development of Er^{3+}-rich core–shell nanostructures. Since 2017, several research groups have independently reported that the inert shell passivation approach is able to remarkably boost the best doping concentration of Er^{3+} from <10% to 100%.[12, 17] Based on this finding, Er^{3+}-rich core–shell nanostructure (e.g., $NaErF_4$@$NaYF_4$ or $NaErF_4$@$NaLuF_4$) has been proposed and constructed. Subsequently, benefitted from the efficient Er^{3+}–Er^{3+} self-sensitization, this type of materials perform robust UC emissions under the 800, 980, or 1530 nm multi-wavelength excitations,[18] According to the previous report,[12] their UC efficiencies are already close to that of the conventionally optimized low-doping systems (e.g., $NaYF_4$: 20%Yb, 2%Er@$NaYF_4$ nanostructure). Besides, these materials also possess a strong signal response to MRI/CT measurements.[19] Therefore, Er^{3+}-rich core–shell nanostructures have attracted numerous research interests, especially in the fields like multi-modal bio-imaging[20] and bio-therapy,[21] trace impurity detection,[22] and solar energy exploitation,[23] etc.

Very recently, a significant breakthrough toward the widely used Er^{3+}-rich core–shell structures has been achieved. Specifically, we and co-workers found that via employing a cryogenic field (e.g., 40 K) to suppress the system's phonon activity, the harmful Er^{3+}–Er^{3+} cross relaxation (CR) will also be strongly restricted, subsequently, the UC brightness of Er^{3+}-rich nanosystem (e.g., $NaErF_4$@$NaYF_4$) can be significantly boosted by around two orders of magnitude.[24] Clearly, standing on this progress, a promising idea is to further combine the positive effect of the cryogenic field with other enhancement approaches together, which may boost the UC brightness to an unprecedented level. One natural design is the

development of a cryogenic luminescent core@active shell@inert shell sandwich structure. As shown in **Figure** 1, due to the energy injection from the active shell to the luminescent core, this structure is proposed to improve the photoluminescence (PL) brightness of the Er^{3+}-rich core. Notably, the effectiveness of active shell design has already been testified in many different UC structures, including the Ln high-doping and Ln low-doping cases.[10, 25] However, almost all the previous reports only focused on the situation at room temperature, in the meantime, the working effectiveness of the active shell in a low-temperature remains unclear.

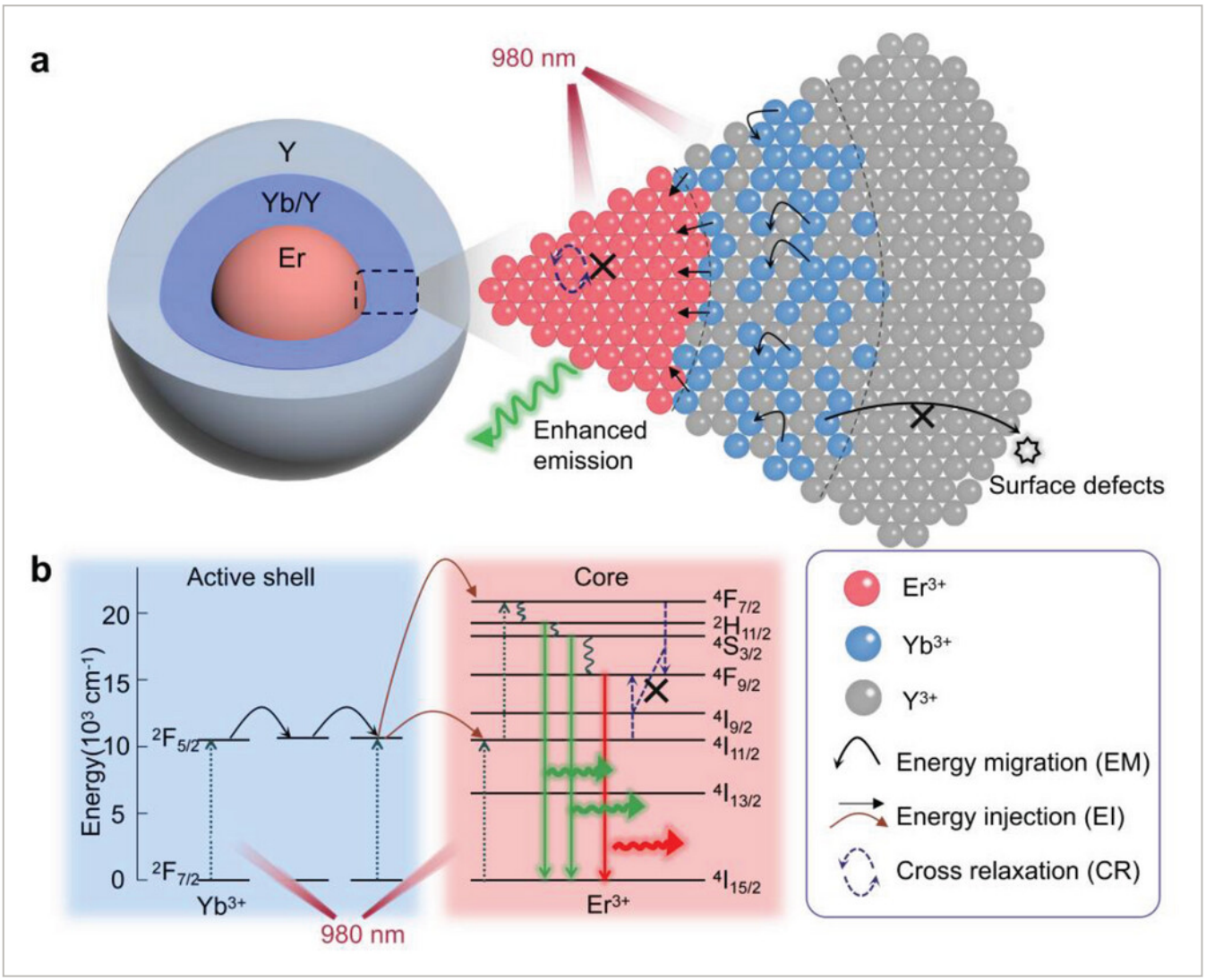

Figure 1

Open in figure viewer | PowerPoint

a) Schematic illustration of the UC processes in cryogenic $NaErF_4$@$NaYF_4$:Yb@$NaYF_4$ nanocrystals. b) Schematic diagram of the energy injection from Yb^{3+} shell to Er^{3+} core (980 nm excitation).

Here in this work, we demonstrated that within a wide temperature range (40–300 K), the inserting of the active shell ($NaYF_4$: x% Yb, x: 0–100) consistently benefits the UC emission of Er^{3+}-rich core-inert shell nanostructure. Taking the Yb^{3+}-freed nanostructure (i.e., Er@Y,

short for $NaErF_4$@$NaYF_4$) as a control, impressive UC improvements (8.3–73-folds) can be observed in Er@Yb@Y nanostructures (short for $NaErF_4$@$NaYbF_4$@$NaYF_4$) via 1) tuning the Yb^{3+} concentration in the active shell (0–100 mol%), and 2) varying the active shell thickness (0-6.0 nm). Moreover, the temperature dependent energy injection effectiveness (from active shell to core) is solidly confirmed by the spectral-domain and time-domain spectroscopic results. Furthermore, we designed a proof-of-concept experiment to testify the potential of Er@Yb@Y nanostructure on temperature related high-security level information encryption. Our results are significant for the deeper understanding and better design of the Er^{3+}-rich UC nanostructures in temperature-related applications.

2 Results and Discussion

The series Er@x%Yb@Y (short for $NaErF_4$@$NaYF_4$: x%Yb@$NaYF_4$, x: 0–100) core–shell–shell nanoparticles are prepared by a successive epitaxial growth strategy.[26] The uniformed morphology and size of bare core ($NaErF_4$), core–shell ($NaErF_4$@$NaYF_4$:x%Yb) and core–shell-shell (Er@x%Yb@Y) structures are confirmed by the TEM and SEM images (Figure 2a–c; Figures S1–S5, Supporting Information), where the diameter/thickness of the inner core, intermediate layer, and outer shell are testified to be ≈17.8, ≈5.8, and ≈6.6 nm, respectively (Tables S1 and S2, Supporting Information). Besides, the pure hexagonal phase of the synthesized nanoparticles was testified by the XRD measurements (Figure S6, Supporting Information). Notably, further characterizations clearly demonstrate that the lanthanide elements' distribution in these synthesized nanostructures well agrees with our design, which guarantees the high quality of our samples. Taking the Er@100%Yb@Y structure as an example, as shown in Figure 2b, the heavy/light lanthanide elements can be clearly distinguished by the brightness of HAADF-STEM imaging (i.e., Er and Yb are located in the internal brighter part, while Y is located in the outside darker part). Besides, the core–shell–shell structure of our sample is also solidly confirmed by the element mappings result (Figure 2d). In addition, the energy dispersive spectroscopy (EDS element analysis) results of the synthesized nanoparticles are also displayed in Figure S7 (Supporting Information), which further confirms the success of the variation of Yb^{3+} concentration in the middle layer (0–100%).

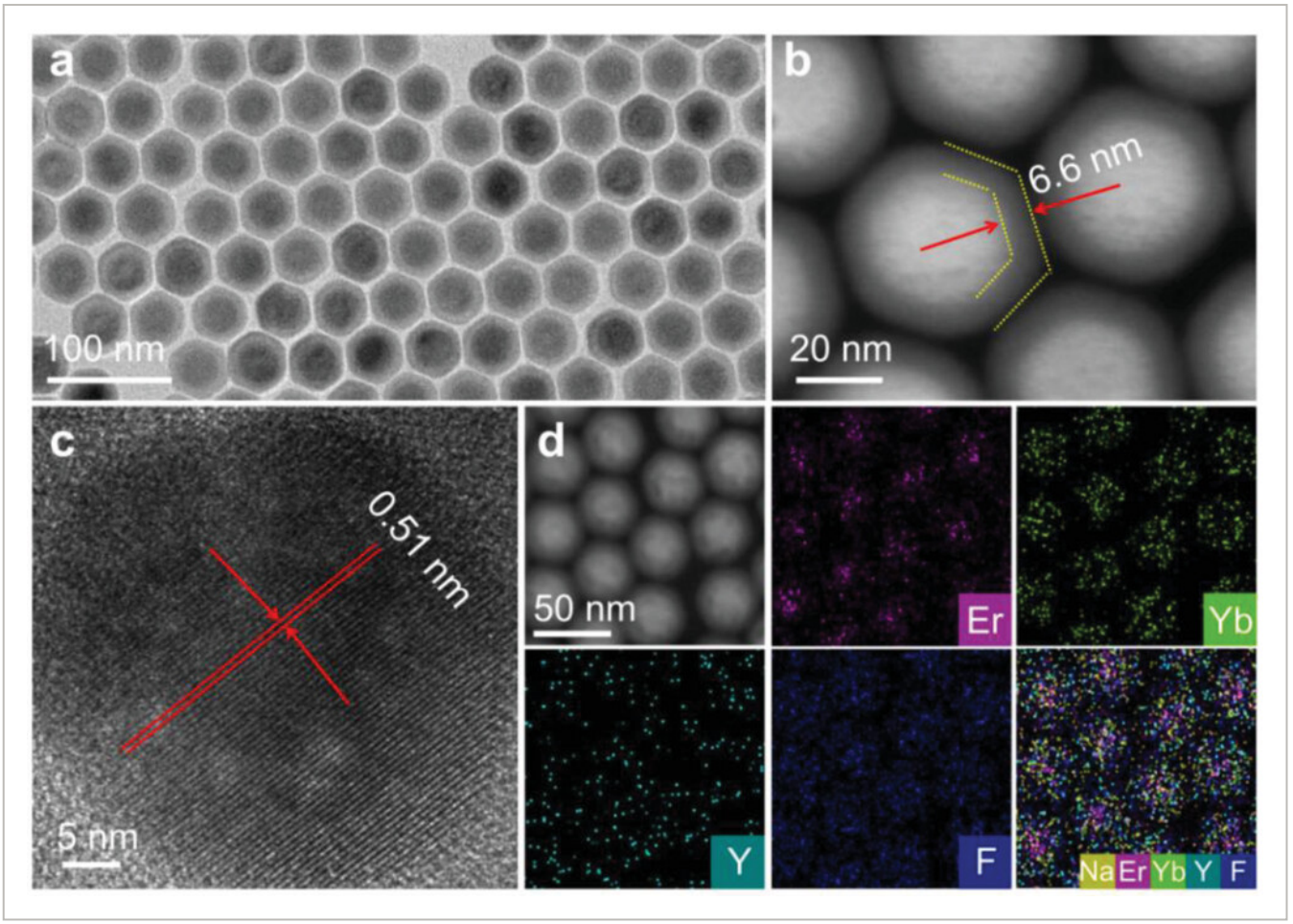

Figure 2

Open in figure viewer | PowerPoint

Sample characterization of synthesized core–shell–shell nanoparticles. a) TEM image of Er@100%Yb@Y structure. b) HAADF-STEM image of Er@100%Yb@Y structure. c) High-resolution TEM image of one Er@100%Yb@Y nanoparticle. d) Scanning TEM image and element mappings of Er, Yb, Y, and F (in Er@100%Yb@Y nanostructure), and an overlap of them (yellow dots represent Na element).

Next, we focused on the critical role of the Yb^{3+} active layer in the Er@Yb@Y nanostructures (i.e., the $NaErF_4$@$NaYF_4$: x%Yb(y nm)@$NaYF_4$ nanostructure). To exclude the potential influences of surface quenchers in advance, an enough thick inert outer layer (6.4–6.9 nm $NaYF_4$) was employed on each sample. On this basis, two important factors, i.e., Yb^{3+} concentration (x: 0–100%) and Yb^{3+} layer thickness (y: 0–6.0 nm), were systematically investigated. Clearly, according to our results (**Figure** 3; Figures S8–S15, Supporting Information), introducing Yb^{3+} in the active layer (i.e., the middle layer) always benefits to the UC intensity in all the interested temperature range, i.e., 40–300 K. Moreover, the more amount of Yb^{3+} was added, the larger the observed UC enhancement (all the samples take the Yb^{3+}-freed Er@Y structure as the control). Specifically, in Figure 3a,b, the Yb^{3+} layer thickness was fixed to 5.8 nm. With the Yb^{3+} concentration increased from 25% to 100% (i.e., x = 25, 50, 75, 100, respectively), the active shell triggered UC enhancement can be observed

in all the involved temperature range. However, the relevant enhancement factors gradually decline with the temperature decreases. At room temperature (300 K), the corresponding UC intensities are calculated to be ≈9.4, 24, 30, 50 times higher than the Er@Y control group, which are well in line with the previous reports.[10] Notably, at 40 K, the enhancement factors fall to 4.9-, 6.9-, 8.4-, 11-folds, respectively. A similar trend reappeared in Figure 3c,d, where the Yb^{3+} concentration was fixed to 100%, and the $NaYbF_4$ shell thickness was precisely tuned to 1.8, 3.8, and 6.0 nm, respectively. At room temperature, the UC enhancements caused by 1.8–6.0 nm $NaYbF_4$ active shell reach 9.5-, 15-, and 73-folds, respectively (also taking the Yb^{3+}-freed Er@Y structure as the control). While at 40 K, the corresponding enhancement factors significantly reduce to 2.7-, 3.8-, and 8.3-folds, respectively. All these results indicate that inserting ≈6 nm $NaYbF_4$ active layer into the traditional Er@Y structure consistently benefits the UC intensity, which is able to further increase the maximum UC brightness ≈1–2 orders of magnitude (i.e., 8.3–73-folds).

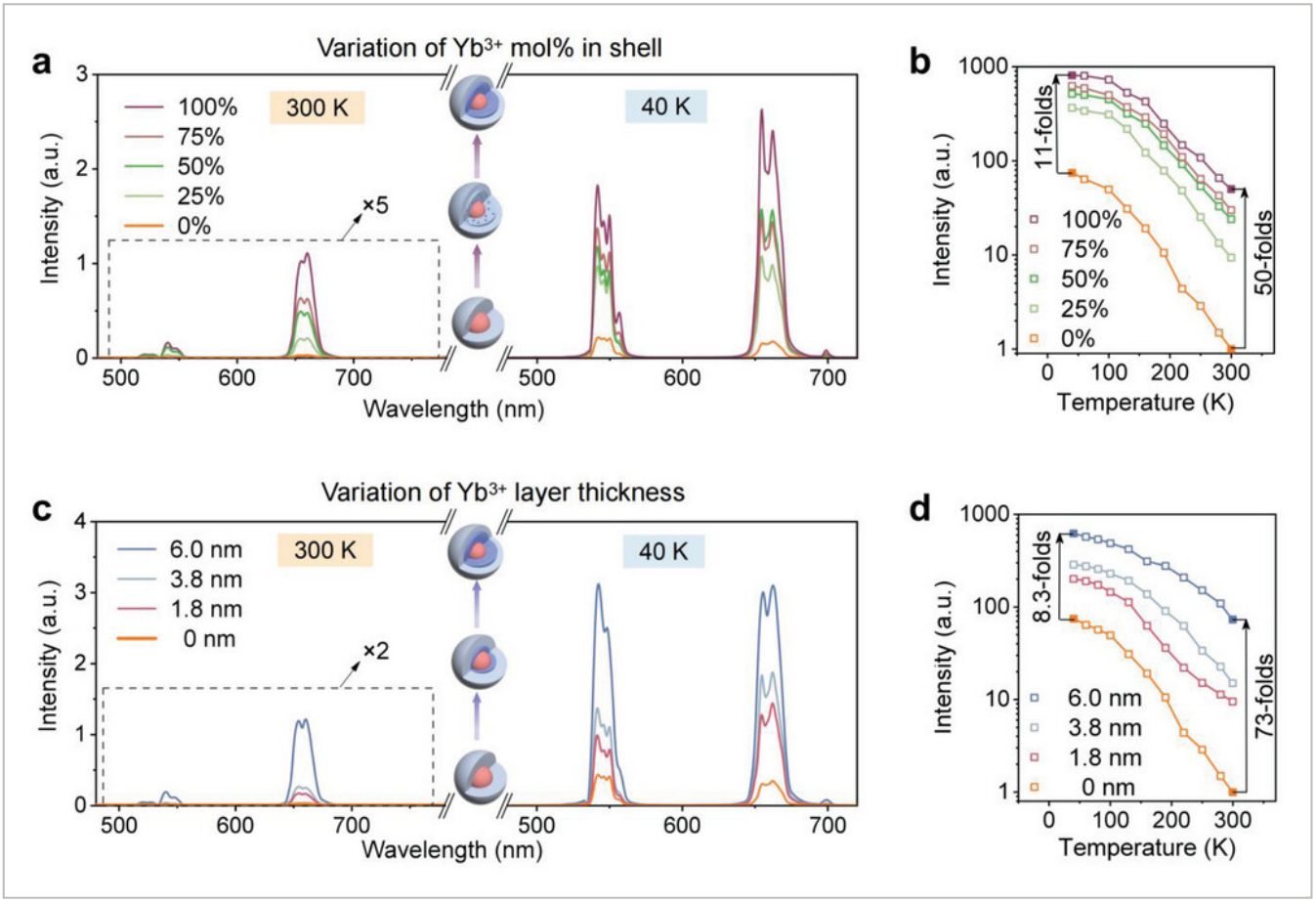

Figure 3

Open in figure viewer | PowerPoint

The steady-state emission spectra of two series UCNPs under 980 nm laser irradiation (0.89 W cm^{-2}). a) UC luminescence spectra of series Er@x%Yb@Y nanostructures (with varied Yb^{3+} doping concentrations, x = 0, 25, 50, 75, and 100 respectively, environmental temperatures are 300 and 40 K, respectively). b) The temperature-dependent overall UC intensity (500–700 nm) of the series Er@x%Yb@Y samples. c) UC luminescence spectra of series Er@Yb(y

nm)@Y nanostructures (with varied Yb^{3+} layer thicknesses, y = 0, 1.8, 3.8, and 6.0 respectively, environmental temperatures are 300 and 40 K, respectively). d) The temperature dependent overall UC intensity (500–700 nm) of series Er@Yb(y nm)@Y nanostructures. UCNPs were dispersed in cyclohexane, and all the observed UC emission intensities were normalized by the numbers of particles.

Next, we move to a deeper understanding to the temperature role on UC enhancement. As mentioned above (shown in Figure 3d), the UC enhancement factor induced by ≈6 nm $NaYbF_4$ active layer (i.e., Er@Yb@Y structure vs Er@Y structure) strongly decreases from 73 to 8.3 with the working temperature decreasing from 300 to 40 K. In our opinion, this difference can be mainly attributed to the two following effects: 1) Low temperature will hinder the energy injection from Yb^{3+} shell to Er^{3+} core. As shown in Figure 4a, there was an energy gap between the two lowest crystal-field components of the Yb^{3+} ions (i.e., $^2F_{5/2}|1>$ and $^2F_{5/2}|0>$). Since the energy transfer from the $^2F_{5/2}|1>$ state of Yb^{3+} to Er^{3+} is much more efficient,[27] low temperature is thus poisonous to the $Yb^{3+}\rightarrow Er^{3+}$ energy transfer efficiency because it will reduce the proportion of the $^2F_{5/2}|1>$ state. Notably, this assumption can be further confirmed by the temperature dependent emission of $NaYF_4$: 20%Yb, 2%Er@$NaYF_4$ nanostructure. As shown in Figure S16 (Supporting Information), the UC intensity is peaking at ≈160 K, which reflects the balance of two competitive effects in low temperature: the decreased energy loss caused by non-radiation transitions and the declined energy transfer efficiency from Yb^{3+} to Er^{3+}. 2) The UC emission of a cryogenic system is more easily to be "saturated". Specifically, in an ideal case, the energy injection process (from Yb^{3+} shell to Er^{3+} core) can be simulated by rising the 980 nm excitation power (i.e., P) in the Er@Y nanostructure. However, due to the so-called "saturation effect", the cryogenic system will have a relatively weak response to the increased excitation power since its emission intensity is already 1–2 orders of magnitude higher than the contestant (the UC emission in the room temperature). Indeed, as shown in Figure 4b, we measured the I–P curves (i.e., $I = p^n$) of Er@Y nanostructure in different temperatures, and the fitted "n" value at 40 K (n_1 = 0.71) is much smaller than it is at 300 K (n_2 = 1.80). Because of the "saturation effect", even taking a temperature non-related energy injection effectiveness (i.e., from Yb^{3+} shell to Er^{3+} core) into the calculation, the calculated UC enhancement at 300 K will still be much larger than the case at 40 K, i.e., $p^{n2} > p^{n1}$ ($n_2 > n_1$). Notably, despite these two negative effects, for the cryogenic Er@Yb@Y sandwich nanostructure, its UC intensity is still around tenfolds higher than that of the cryogenic Er@Y structure (i.e., 11-folds in Figure 3b and 8.3-folds in Figure 3d), which demonstrates the success of our original design, i.e., the combination of 1) Yb^{3+} sensitization effect, and 2) the cryogenic field induced CR suppression, is able to further promote the UC brightness of traditional Er^{3+}-rich core-inert shell nanostructures.

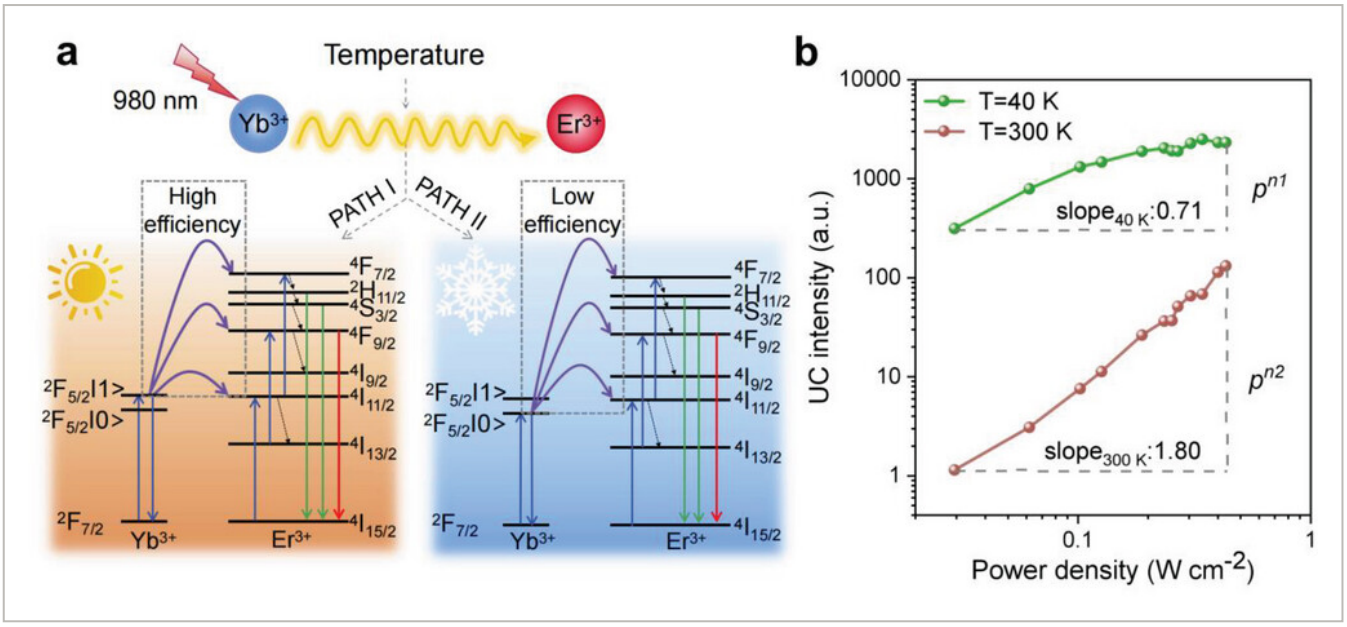

Figure 4

Open in figure viewer | PowerPoint

a) Schematic diagram of the temperature-dependent Yb^{3+}→Er^{3+} transitions (under 980 nm excitation). The former (PATH I) represents the case in the room temperature and the latter (PATH II) shows the case in the cryogenic environment. b) The measured log–log plots of UC emission intensity (from $NaErF_4$@$NaYF_4$ nanostructure) versus the employed 980 nm laser pumping power density, the green line (at 40 K) and the dull-red line (at 300 K) present the measured results in different environmental temperatures.

To further determine the PL dynamics of Yb^{3+}→Er^{3+} (shell→core) energy injection, we investigated the time-domain UC spectra when the series samples were excited by the nanosecond pulses. Notably, here we chose a 940 nm pulse (rather than the traditional 980 nm) to excite the series samples. As shown in Figure 5a, the employ of 940 nm excitation enables us to perfectly separate the absorption (Yb^{3+} active layer) and emission (Er^{3+} core) regions in the Er@Yb@Y sandwich structure. Since the Er^{3+} in the core area cannot be excited by 940 nm (Figure S17, Supporting Information), the observed UC emission will completely rely on the Yb^{3+}→Er^{3+} (shell→core) energy transfer. According to our previous report,[28] for this "absorption–emission" fully spatial separated nanostructure, because of the influence of Yb^{3+}–Yb^{3+} energy migration time in the middle active layer, the averaged energy injection time from sensitizer (Yb^{3+}) to activator (Er^{3+}) can be precisely tuned by 1) the thickness of the Yb^{3+} layer, or 2) the Yb^{3+} dopant concentration. As a result, the rise edge of the measured dynamic curves will be regularly tuned. Indeed, as shown in Figure 5b, for the 540 nm UC dynamic curves (i.e., the $^4S_{3/2}$ → $^4I_{15/2}$ transition of Er^{3+}), increasing the thickness of Yb^{3+} layer (i.e., $NaYbF_4$) from 1.8 to 6.0 nm results in prolongation of rise edge from 10 to 17 μs, which can be attributed to the increased Yb^{3+}–Yb^{3+} energy migration distance. A similar trend has also been observed in Figure 5c, in which the rise edge modulation from 14 to 50 μs has been achieved by decreasing the Yb^{3+}

concentration from 100% to 25% (in these series samples, the Yb^{3+} layer thicknesses are fixed to 5.8 nm). It is worth noticing that decreasing Yb^{3+} dopant concentration triggers two opposite effects simultaneously. On one side, it decreases the Yb^{3+}–Yb^{3+} energy migration rate significantly due to the enlarged ion-to-ion distance, which delays the energy injection time. On the other side, the sparse ion distribution in the active layer can reduce the required Yb^{3+}–Yb^{3+} plies to be traversed during the energy injection (since the active layer is fixed to 5.8 nm), and speeds up the energy injection. From our results, the former effects cover the latter effects, which explains the prolonged rise edge with the decreased Yb^{3+} concentration (Figure 5c). Overall, all these dynamic results unambiguously confirm the existence of $Yb^{3+}\rightarrow Er^{3+}$ energy injection, which is well in line with our observed steady-state results.

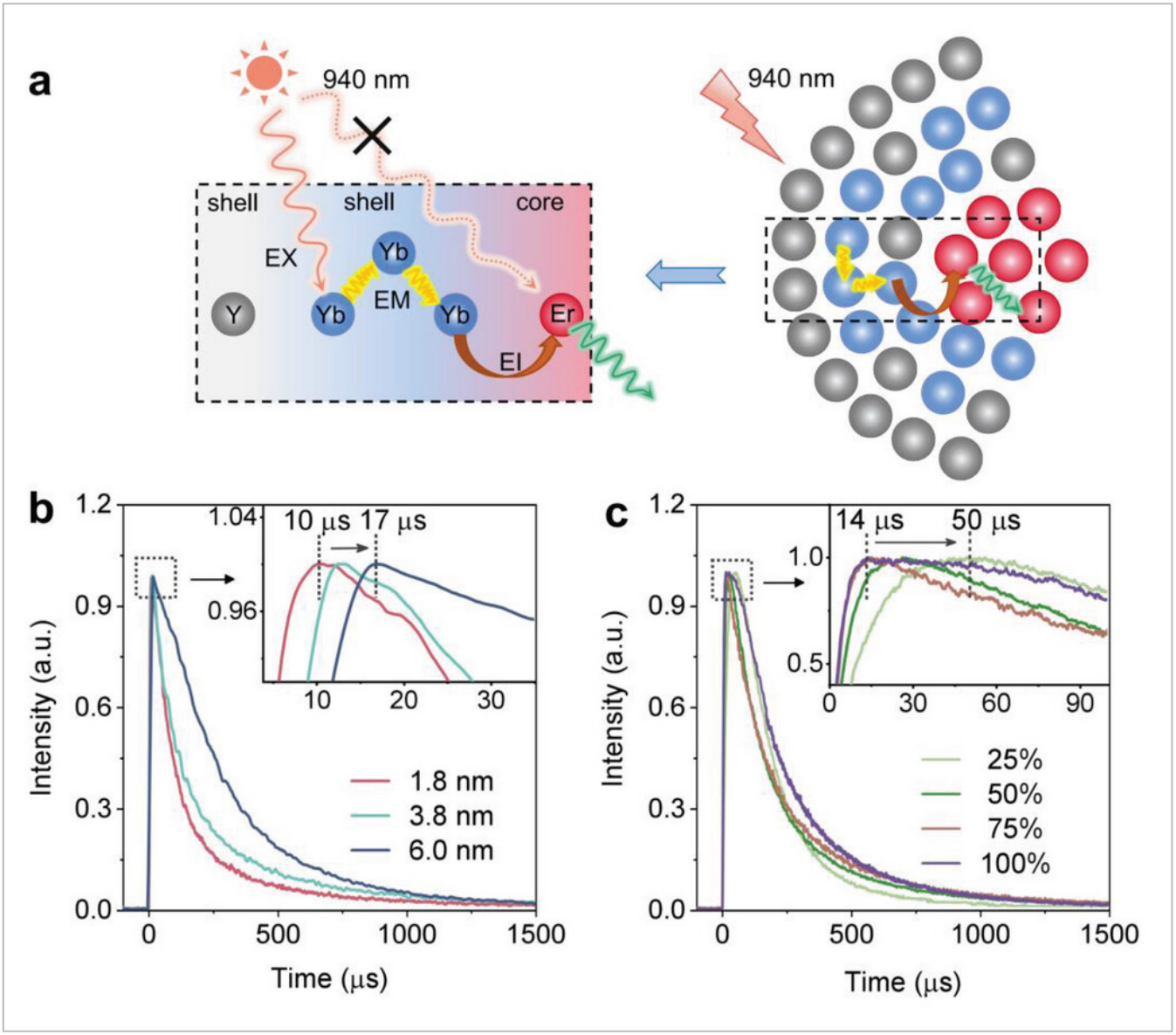

Figure 5

Open in figure viewer | PowerPoint

a) Schematic diagram of the UC processes in Er@Yb@Y core–shell–shell nanostructure (under the 940 nm excitation). b) UC dynamic curves for the Er^{3+}: $^4S_{3/2} \rightarrow {}^4I_{15/2}$ transition in the Er@100%Yb@Y nanostructures with variable Yb^{3+} layer thickness (1.8–6.0 nm). c) UC dynamic curves for the Er^{3+}: $^4S_{3/2} \rightarrow {}^4I_{15/2}$ transition in the Er@x%Yb (5.8 nm) @Y nanostructures with variable Yb^{3+} doping concentrations (*x*: 25–100). The illustrations in (b,c) show the enlarged portion of the rise edge of the curves.

Interestingly, the cryogenic field induced significant UC enhancement will be invalid by adding Tm^{3+} (e.g., 0.5%) into the Er^{3+}-rich core. As shown in the Figure 6a, the $NaErF_4$: 0.5%Tm@$NaYF_4$ system (named as ErTm@Y, 18.3 nm core with 6.7 nm shell, shown in Figure S18, Supporting Information) performs only ≈3.4-folds UC variation when the temperature decreases from 300 to 40 K. As a stark contrast, under the same excitation condition, 1–2 orders of magnitude UC enhancement can be observed in the Tm^{3+}-free samples (i.e., Er@Y or Er@Yb@Y systems, shown in Figures S8 and S15, Supporting Information). Furthermore, along with the UC enhancement regulation, Tm^{3+} also has a great influence on the output red/green (R/G) emission ratio. As shown in Figure 6b, unlike the Er@Y or Er@Yb(6 nm)@Y systems, which perform a relatively strong green emission (i.e., low R/G emission ratio) in the low temperature due to the green→red CR suppression, only for the ErTm@Y system, extremely high R/G emission ratio (>10) remains at all the interested temperatures (*T*: 40–300 K). These two unique phenomena can be well attributed to the influence of Er^{3+}–Tm^{3+} interactions, which rebuild the excited state depopulation channels of Er^{3+}. Specifically, as shown in Figure 6c, due to the "trap" role of Tm^{3+} (i.e., the Er^{3+}–Tm^{3+} interactions), even in the presence of cryogenic temperature, efficient depopulation from the green and red emitting energy levels of Er^{3+} still exists, which explains the relatively weak UC enchantment and the relatively large R/G ratio in the cryogenic ErTm@Y system.

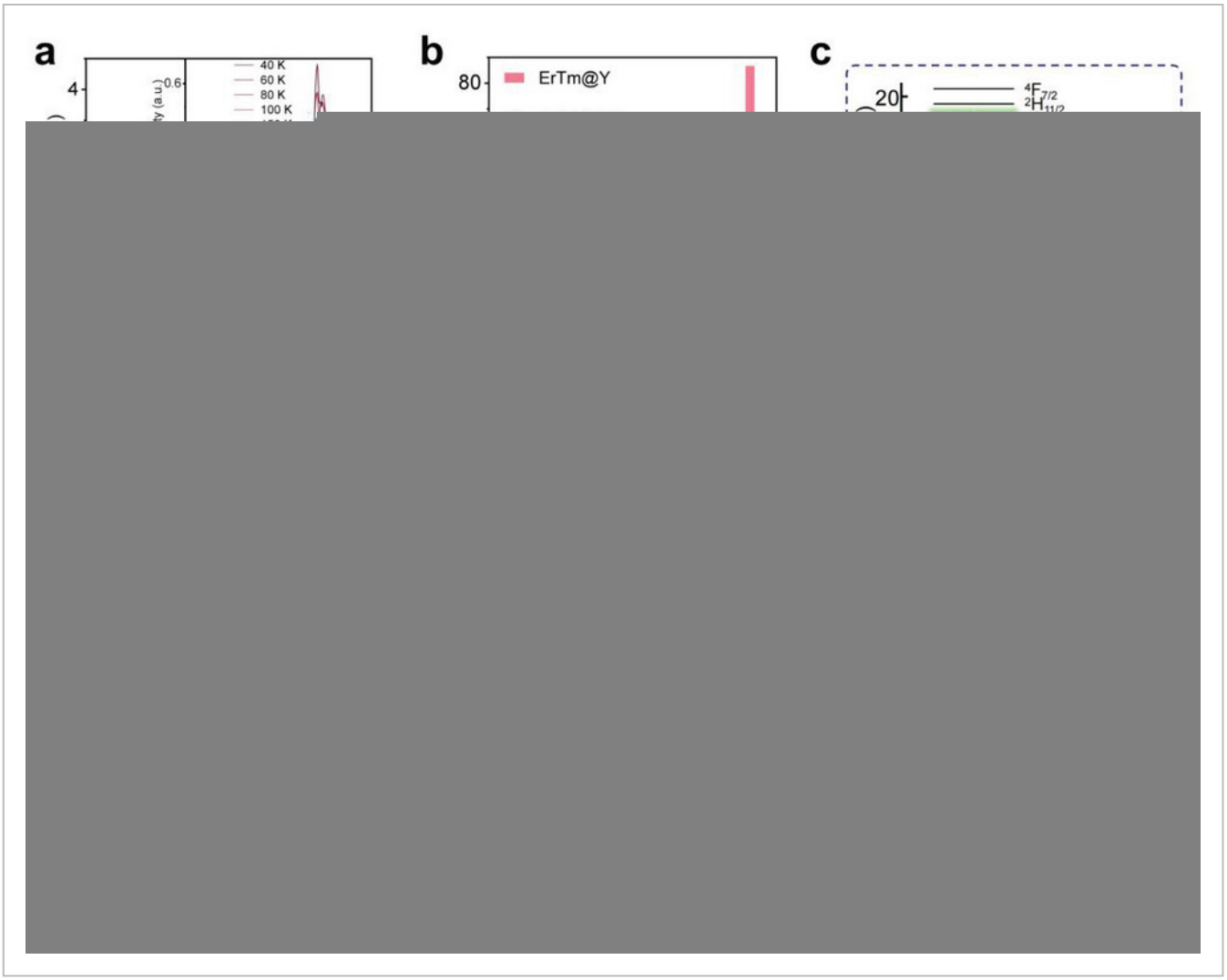

Figure 6

Open in figure viewer | PowerPoint

a) Temperature dependent (40–300 K) UC emission intensity of $NaErF_4$: Tm (0.5 mol.%)@$NaYF_4$ nanostructure (980 nm excitation, 0.89 W cm^{-2}). The illustration shows the steady-state UC emission spectra at different temperatures. b) The measured R/G emission ratios of ErTm@Y, Er@Yb(6 nm)@Y, and Er@Y nanostructures at different temperatures. c) Proposed Er^{3+}–Tm^{3+} interactions which efficiently depopulate the excited states on relevant UC emitting energy levels. d) A proof-of-concept experiment of temperature-induced high-level information encryption application, where a quick response (QR) code is made of Er@Yb(6 nm)@Y nanoparticles and covered with an interference layer (i.e., ErTm@Y), and the temperature-controlled PL of the QR code are displayed in the picture.

Notably, based on the significantly different temperature responses of Tm^{3+}- involved and noninvolved systems, a schematic temperature-induced information encryption application is demonstrated here. As shown in Figure 6d, a quick response (QR) code is generated by stamping the Tm^{3+}-free UCNPs (i.e., our designed Er@Yb@Y) on a paper. Subsequently, this QR code is covered by another Tm^{3+}- involved interference layer, i.e., ErTm@Y nanoparticles. In sunlight, the entire QR code pattern is invisible. At room temperature, under the

excitation of 980 nm, despite the signal area appearing, no identifiable signals can be observed due to the existence of the interference layer (i.e., red dazzling light from ErTm@Y UCNPs). However, with the temperature decreasing to 77 K (assisted by liquid nitrogen), due to the significantly boosted green emission intensity of the Er@Yb@Y UCNPs, green image of the QR code with high spatial resolution is successfully obtained (Figure 6d; Video S1, Supporting Information), and the concealed information can be read directly by a commercial mobile phone application (e.g., We Chat). Considering that there are relatively few UCNPs that have a significant response to cryogenic field,[29] our work offers more alternatives to promote the future relevant applications of low-temperature-induced information encryption.

3 Conclusion

In summary, we confirm that within a wide temperature range (40–300 K), inserting a Yb^{3+} active layer into the traditional Er^{3+}-rich core-inert shell nanostructure (e.g., $NaErF_4$@$NaYF_4$) will consistently benefit the UC intensity. Spectral-domain and time-domain spectroscopic results indicate that the observed UC enhancement (8.3–73-folds) is caused by the energy injection from the active Yb^{3+} shell to the Er^{3+} core. More importantly, we demonstrate that the energy injection effectiveness is strongly modulated by the environment temperature. Furthermore, based on the largely tunable UC emission intensity and the output color variation of our optimized nanostructure (i.e., $NaErF_4$@$NaYbF_4$@$NaYF_4$), a conceptual model of the QR code information encryption is successfully provided. Our results shed light on more dimensional control for the migrated energy in the complex multi-layer nanostructures and provide more alternatives for the temperature-related applications of lanthanide based UCNPs.

Acknowledgements

This research was supported by the National Natural Science Foundation of China (Grants Nos. 12104179, 62105031, 62075217), the Fundamental Research Funds for the Central Universities, Jilin University, and the Project of Science and Technology Agency, Jilin Province (20210101148JC, 20230508104RC).

Conflict of Interest

The authors declare no conflict of interest.

Open Research

Data Availability Statement

The data that support the findings of this study are available from the corresponding author upon reasonable request.

Supporting Information

Filename	Description
adom202301827-sup-0001-SuppMat.pdf 1 MB	Supporting Information
adom202301827-sup-0002-VideoS1.mp4 1,011.7 KB	Supplemental Video 1

Please note: The publisher is not responsible for the content or functionality of any supporting information supplied by the authors. Any queries (other than missing content) should be directed to the corresponding author for the article.

References

1 a) J. Huang, L. Yan, S. Liu, L. Tao, B. Zhou, *Mater. Horiz.* 2022, **9**, 1167;

CAS | PubMed | Web of Science® | Google Scholar

b) M. Haase, H. Schafer, *Angew. Chem., Int. Ed.* 2011, **50**, 5808;

CAS | PubMed | Web of Science® | Google Scholar

c) F. Auzel, *Chem. Rev.* 2004, **104**, 139.

CAS | PubMed | Web of Science® | Google Scholar

2 a) K. Du, J. Feng, X. Gao, H. Zhang, *Light Sci. Appl.* 2022, **11**, 222;

CAS | PubMed | Web of Science® | Google Scholar

b) H. Li, X. Liu, D. Zhou, B. Dong, L. Xu, X. Bai, H. Song, *Adv. Mater.* 2023, **35**, 2300118;

CAS | Google Scholar

c) Y. Zhuang, D. Chen, W. Chen, W. Zhang, X. Su, R. Deng, Z. An, H. Chen, R. J. Xie, *Light Sci. Appl.* 2021, **10**, 132.

CAS | PubMed | Web of Science® | Google Scholar

3 a) Z. Yi, Z. Luo, X. Qin, Q. Chen, X. Liu, *Acc. Chem. Res.* 2020, **53**, 2692;

CAS | PubMed | Web of Science® | Google Scholar

b) J. Zhou, M. X. Yu, Y. Sun, X. Z. Zhang, X. J. Zhu, Z. H. Wu, D. M. Wu, F. Y. Li, *Biomaterials* 2011, **32**, 1148;

CAS | PubMed | Web of Science® | Google Scholar

c) C. Li, J. Lin, *J. Mater. Chem.* 2010, **20**, 6831.

CAS | Web of Science® | Google Scholar

4 a) F. Wang, X. Liu, *Chem. Soc. Rev.* 2009, **38**, 976;

CAS | PubMed | Web of Science® | Google Scholar

b) Z. Wei, Y. Liu, B. Li, J. Li, S. Lu, X. Xing, K. Liu, F. Wang, H. Zhang, *Light Sci. Appl.* 2022, **11**, 175.

CAS | PubMed | Web of Science® | Google Scholar

5 a) R. Deng, F. Qin, R. Chen, W. Huang, M. Hong, X. Liu, *Nat. Nanotechnol.* 2015, **10**, 237;

CAS | PubMed | Web of Science® | Google Scholar

b) K. R. Mun, J. Kyhm, J. Y. Lee, S. Shin, Y. Zhu, G. Kang, D. Kim, R. Deng, H. S. Jang, *Nano Lett.* 2023, **23**, 3014;

CAS | PubMed | Web of Science® | Google Scholar

c) H. Na, K. Woo, K. Lim, H. S. Jang, *Nanoscale* 2013, **5**, 4242.

CAS | PubMed | Web of Science® | Google Scholar

6 a) J. Huang, Z. An, L. Yan, B. Zhou, *Adv. Funct. Mater.* 2023, **33**, 2212037;

CAS | Web of Science® | Google Scholar

b) H. Xiao, B. Liu, L. Qiu, G. Li, G. Zhang, D. Huang, Y. Zhao, C. Yang, F. Jiang, P. Dang, H. Lian, Z. Cheng, J. Lin, *Angew. Chem., Int. Ed.* 2022, **61**, e202115136;

CAS | PubMed | Web of Science® | Google Scholar

c) Y. Liu, G. Pan, H. Gao, H. Zhang, T. Ao, W. Gao, Y. Mao, *Ceram. Int.* 2021, **47**, 18824;

CAS | Web of Science® | Google Scholar

d) H. Huang, J. Chen, Y. Liu, J. Lin, S. Wang, F. Huang, D. Chen, *Small* 2020, **16**, e2000708;

CAS | PubMed | Web of Science® | Google Scholar

e) W. Yao, Q. Tian, B. Tian, M. Li, H. Wang, P. Zeng, L. Liu, H. Zheng, W. Wu, *Sci. China Mater.* 2018, **62**, 368.

Web of Science® | Google Scholar

7 a) B. Zhou, B. Tang, C. Zhang, C. Qin, Z. Gu, Y. Ma, T. Zhai, J. Yao, *Nat. Commun.* 2020, **11**, 1174;

CAS | PubMed | Web of Science® | Google Scholar

b) A. Pliss, T. Y. Ohulchanskyy, G. Chen, J. Damasco, C. E. Bass, P. N. Prasad, *ACS Photonics* 2017, **4**, 806;

CAS | Web of Science® | Google Scholar

c) G. Y. Chen, H. L. Qju, P. N. Prasad, X. Y. Chen, *Chem. Rev.* 2014, **114**, 5161.

CAS | PubMed | Web of Science® | Google Scholar

8 a) Q. Zhan, H. Liu, B. Wang, Q. Wu, R. Pu, C. Zhou, B. Huang, X. Peng, H. Gren, S. He, *Nat. Commun.* 2017, **8**, 1058;

PubMed | Web of Science® | Google Scholar

b) Y. Liu, Y. Lu, X. Yang, X. Zheng, S. Wen, F. Wang, X. Vidal, J. Zhao, D. Liu, Z. Zhou, C. Ma, J. Zhou, J. A. Piper, P. Xi, D. Jin, *Nature* 2017, **543**, 229;

CAS | PubMed | Web of Science® | Google Scholar

c) C. Lee, E. Z. Xu, Y. W. Liu, A. Teitelboim, K. Y. Yao, A. Fernandez-Bravo, A. M. Kotulska, S. H. Nam, Y. D. Suh, A. Bednarkiewicz, B. E. Cohen, E. M. Chan, P. J. Schuck, *Nature* 2021, **589**, 230.

CAS | PubMed | Web of Science® | Google Scholar

9 a) Y. Feng, Z. Li, Q. Li, J. Yuan, L. Tu, L. Ning, H. Zhang, *Light Sci. Appl.* 2021, **10**, 105;

CAS | PubMed | Web of Science® | Google Scholar

b) B. Chen, F. Wang, *Trends Chem.* 2020, **2**, 427.

CAS | Google Scholar

10 a) H. Lin, D. Xu, Z. Cheng, Y. Li, L. Xu, Y. Ma, S. Yang, Y. Zhang, *Appl. Surf. Sci.* 2020, **514**, 146074;

CAS | Google Scholar

b) T. Sun, Y. Li, W. L. Ho, Q. Zhu, X. Chen, L. Jin, H. Zhu, B. Huang, J. Lin, B. E. Little, S. T. Chu, F. Wang, *Nat. Commun.* 2019, **10**, 1811;

PubMed | Web of Science® | Google Scholar

c) D. Ahiboz, E. Andresen, P. Manley, U. Resch-Genger, C. Würth, C. Becker, *Adv. Opt. Mater.* 2021, **9**, 2101285;

CAS | Web of Science® | Google Scholar

d) L. Lyu, H. Cheong, X. Ai, W. Zhang, J. Li, H. Yang, J. Lin, B. Xing, *NPG Asia Mater* 2018, **10**, 685;

Web of Science® | Google Scholar

e) Y. Yao, C. Xu, Y. Zheng, C. Yang, P. Liu, J. Ding, T. Jia, J. Qiu, S. Zhang, Z. Sun, *J. Mater. Sci.* 2016, **51**, 5460.

CAS | Web of Science® | Google Scholar

11 J. C. Boyer, F. C. van Veggel, *Nanoscale* 2010, **2**, 1417.

CAS | PubMed | Web of Science® | Google Scholar

12 a) J. Zuo, Q. Li, B. Xue, C. Li, Y. Chang, Y. Zhang, X. Liu, L. Tu, H. Zhang, X. Kong, *Nanoscale* 2017, **9**, 7941;

CAS | PubMed | Web of Science® | Google Scholar

b) S. Wen, J. Zhou, K. Zheng, A. Bednarkiewicz, X. Liu, D. Jin, *Nat. Commun.* 2018, **9**, 2415;

PubMed | Web of Science® | Google Scholar

c) B. Chen, F. Wang, *Acc. Chem. Res.* 2020, **53**, 358;

CAS | PubMed | Web of Science® | Google Scholar

d) B. Tian, A. Fernandez-Bravo, H. Najafiaghdam, N. A. Torquato, M. V. P. Altoe, A. Teitelboim, C. A. Tajon, Y. Tian, N. J. Borys, E. S. Barnard, M. Anwar, E. M. Chan, P. J. Schuck, B. E. Cohen, *Nat. Commun.* 2018, **9**, 3082.

PubMed | Web of Science® | Google Scholar

13 J. Zhao, D. Jin, E. P. Schartner, Y. Lu, Y. Liu, A. V. Zvyagin, L. Zhang, J. M. Dawes, P. Xi, J. A. Piper, E. M. Goldys, T. M. Monro, *Nat. Nanotechnol.* 2013, **8**, 729.

CAS | PubMed | Web of Science® | Google Scholar

14 a) W. Wei, G. Chen, A. Baev, G. S. He, W. Shao, J. Damasco, P. N. Prasad, *J. Am. Chem. Soc.* 2016, **138**, 15130;

CAS | PubMed | Web of Science® | Google Scholar

b) B. Xue, D. Wang, Y. Zhang, J. Zuo, Y. Chang, L. Tu, X. Liu, Z. Yuan, H. Zhao, J. Song, J. Qu, X. Kong, *J. Mater. Chem. C* 2019, **7**, 8607;

CAS | Web of Science® | Google Scholar

c) W. Q. Zou, C. Visser, J. A. Maduro, M. S. Pshenichnikov, J. C. Hummelen, *Nat. Photonics* 2012, **6**, 560;

CAS | Web of Science® | Google Scholar

d) X. Wu, Y. W. Zhang, K. Takle, O. Bilsel, Z. J. Li, H. Lee, Z. J. Zhang, D. S. Li, W. Fan, C. Y. Duan, E. M. Chan, C. Lois, Y. Xiang, G. Han, *ACS Nano* 2016, **10**, 1060.

CAS | PubMed | Web of Science® | Google Scholar

---

15 a) B. Shen, S. M. Cheng, Y. Y. Gu, D. R. Ni, Y. L. Gao, Q. Q. Su, W. Feng, F. Y. Li, *Nanoscale* 2017, **9**, 1964;

CAS | PubMed | Web of Science® | Google Scholar

b) T. Cheng, R. Marin, A. Skripka, F. Vetrone, *J. Am. Chem. Soc.* 2018, **140**, 12890;

CAS | PubMed | Web of Science® | Google Scholar

c) F. Wang, J. Wang, X. Liu, *Angew. Chem., Int. Ed.* 2010, **49**, 7456.

CAS | PubMed | Web of Science® | Google Scholar

---

16 Y. Zhang, R. Wen, J. Hu, D. Guan, X. Qiu, Y. Zhang, D. S. Kohane, Q. Liu, *Nat. Commun.* 2022, **13**, 5927.

CAS | PubMed | Google Scholar

---

17 a) N. J. Johnson, S. He, S. Diao, E. M. Chan, H. Dai, A. Almutairi, *J. Am. Chem. Soc.* 2017, **139**, 3275;

CAS | PubMed | Web of Science® | Google Scholar

b) Q. Chen, X. Xie, B. Huang, L. Liang, S. Han, Z. Yi, Y. Wang, Y. Li, D. Fan, L. Huang, X. Liu, *Angew. Chem., Int. Ed.* 2017, **56**, 7605.

CAS | PubMed | Web of Science® | Google Scholar

---

18 a) J. Huang, L. Yan, S. Liu, N. Song, Q. Zhang, B. Zhou, *Adv. Funct. Mater.* 2021, **31**, 2009796;

CAS | Web of Science® | Google Scholar

b) D. Chen, M. Xu, M. Ma, P. Huang, *Dalton Trans.* 2017, **46**, 15373.

CAS | PubMed | Web of Science® | Google Scholar

---

19 S. He, N. J. J. Johnson, V. A. Nguyen Huu, E. Cory, Y. Huang, R. L. Sah, J. V. Jokerst, A. Almutairi, *Nano Lett.* 2017, **17**, 4873.

CAS | PubMed | Web of Science® | Google Scholar

20 H. Li, X. Wang, X. Li, S. Zeng, G. Chen, *Chem. Mater.* 2020, **32**, 3365.

CAS | Web of Science® | Google Scholar

21 a) S. He, N. J. J. Johnson, H. Viet Anh Nguyen, Y. Huang, A. Almutairi, *Chem. Mater.* 2018, **30**, 3991;

CAS | Web of Science® | Google Scholar

b) J. Zuo, L. Tu, Q. Li, Y. Feng, I. Que, Y. Zhang, X. Liu, B. Xue, L. J. Cruz, Y. Chang, H. Zhang, X. Kong, *ACS Nano* 2018, **12**, 3217.

CAS | PubMed | Web of Science® | Google Scholar

22 L. Liu, S. Wang, B. Zhao, P. Pei, Y. Fan, X. Li, F. Zhang, *Angew. Chem., Int. Ed.* 2018, **57**, 7518.

CAS | PubMed | Web of Science® | Google Scholar

23 a) D. Liu, X. Zhang, W. Qin, B. Yao, L. Tu, Y. Li, G. Wang, H. Luan, X. Kong, Z. Ding, Y. Jiang, H. Zhao, Z. Zhang, L. Zhang, *Sol. Energy Mater. Sol. Cells* 2019, **203**, 110175;

CAS | Google Scholar

b) Y. F. Shang, S. W. Hao, W. Q. Lv, T. Chen, L. Tian, Z. T. Lei, C. H. Yang, *J. Mater. Chem. C* 2018, **6**, 3869.

CAS | Web of Science® | Google Scholar

24 a) L. Tu, K. Wu, Y. Luo, E. Wang, J. Yuan, J. Zuo, D. Zhou, B. Li, J. Zhou, D. Jin, H. Zhang, *Angew. Chem., Int. Ed.* 2023, **62**, e202217100;

CAS | PubMed | Web of Science® | Google Scholar

b) K. Wu, E. Wang, J. Yuan, J. Zuo, D. Zhou, H. Zhao, Y. Luo, L. Zhang, B. Li, J. Zhang, L. Tu, H. Zhang, *Angew. Chem., Int. Ed.* 2023, **62**, e202306585.

CAS | PubMed | Google Scholar

25 a) G. Gong, Y. Song, H. Tan, S. Xie, C. Zhang, L. Xu, J. Xu, J. Zheng, *Composites, Part B* 2019, **179**, 107504;

CAS | Web of Science® | Google Scholar

b) F. Vetrone, R. Naccache, V. Mahalingam, C. G. Morgan, J. A. Capobianco, *Adv. Funct. Mater.* 2009, **19**, 2924.

CAS | Web of Science® | Google Scholar

26 N. J. Johnson, A. Korinek, C. Dong, F. C. van Veggel, *J. Am. Chem. Soc.* 2012, **134**, 11068.

CAS | PubMed | Web of Science® | Google Scholar

27 a) J. F. Suyver, J. Grimm, M. K. van Veen, D. Biner, K. W. Krämer, H. U. Güdel, *J. Lumin.* 2006, **117**, 1;

CAS | Web of Science® | Google Scholar

b) K. Wu, J. Cui, X. Kong, Y. Wang, *J. Appl. Phys.* 2011, **110**, 053510.

CAS | Web of Science® | Google Scholar

28 J. Zuo, D. Sun, L. Tu, Y. Wu, Y. Cao, B. Xue, Y. Zhang, Y. Chang, X. Liu, X. Kong, W. J. Buma, E. J. Meijer, H. Zhang, *Angew. Chem., Int. Ed.* 2018, **57**, 3054.

CAS | PubMed | Web of Science® | Google Scholar

29 a) X. Fan, J. Nie, W. Ying, S. Xu, J. Gu, S. Liu, *Dalton Trans.* 2021, **50**, 12234.

CAS | PubMed | Web of Science® | Google Scholar

b) Q. Li, X. Xie, H. Wu, H. Chen, W. Wang, X. Kong, Y. Chang, *Nano Lett.* 2023, **23**, 3444.

CAS | PubMed | Web of Science® | Google Scholar

c) S. Liu, L. Yan, J. Huang, Q. Zhang, B. Zhou, *Chem. Soc. Rev.* 2022, **51**, 1729.

CAS | PubMed | Web of Science® | Google Scholar